APPLIED SCIENCES AND ENGINEERING

Flexible submental sensor patch with remote monitoring controls for management of oropharyngeal swallowing disorders

Min Ku Kim[1]*, Cagla Kantarcigil[2]*, Bongjoong Kim[3], Ratul Kumar Baruah[4,5], Shovan Maity[4], Yeonsoo Park[3], Kyunghun Kim[1], Seungjun Lee[3], Jaime Bauer Malandraki[2], Shitij Avlani[4], Anne Smith[2], Shreyas Sen[4], Muhammad A. Alam[4], Georgia Malandraki[1,2†], Chi Hwan Lee[1,2,3†]

Successful rehabilitation of oropharyngeal swallowing disorders (i.e., dysphagia) requires frequent performance of head/neck exercises that primarily rely on expensive biofeedback devices, often only available in large medical centers. This directly affects treatment compliance and outcomes, and highlights the need to develop a portable and inexpensive remote monitoring system for the telerehabilitation of dysphagia. Here, we present the development and preliminarily validation of a skin-mountable sensor patch that can fit on the curvature of the submental (under the chin) area noninvasively and provide simultaneous remote monitoring of muscle activity and laryngeal movement during swallowing tasks and maneuvers. This sensor patch incorporates an optimal design that allows for the accurate recording of submental muscle activity during swallowing and is characterized by ease of use, accessibility, reusability, and cost-effectiveness. Preliminary studies on a patient with Parkinson's disease and dysphagia, and on a healthy control participant demonstrate the feasibility and effectiveness of this system.

INTRODUCTION

Successful completion of a swallow requires the precise coordination of more than 40 pairs of muscles of the head and neck, six pairs of cranial nerves, complex circuitry in the brainstem, and several brain areas (*1*–*3*). Any disruption in these pathways can result in oropharyngeal swallowing disorders (also known as oropharyngeal dysphagia). Every year in the United States alone, approximately 9.44 million of adults and more than 500,000 children are reported to experience dysphagia (*4*, *5*). Dysphagia is commonly caused by a variety of neurological conditions (e.g., stroke, cerebral palsy, Parkinson's disease, and dementia), head and neck cancer, and its treatment, trauma, and genetic syndromes (*6*, *7*). Dysphagia interferes with daily life and, without proper treatment, can lead to devastating consequences such as malnutrition, dehydration, respiratory compromise (due to aspiration of food/liquid into the lungs), or even death (*8*, *9*). Current rehabilitative interventions for dysphagia can be effective but require frequent performances of head/neck exercises that primarily rely on expensive biofeedback devices (e.g., oral manometers, electromyographic devices, and endoscopy) (*10*–*13*). The treatment protocols require patients to make multiple visits per day or week to a clinic for treatments, which is often not feasible or economically viable for many patients, especially for those with mobility limitations or living in rural areas that often experience shortages of medical professionals and resources (*14*). Consequently, studies have shown average treatment adherence for swallowing interventions to be between 22 and 52% (*15*), possibly leading to suboptimal treatment and outcomes.

Alternative strategies involve the use of portable monitoring devices to obtain biofeedback signals during swallowing and swallowing maneuvers in a form that allows for real-time data collection or cloud storage for postdata processing (*16*–*19*). However, most currently available devices suffer from rigid or semiflexible platforms that are not suited to interface with the curvilinear surface of the submental area, particularly within the context of head/neck movement, thereby often resulting in poor data acquisition and discomfort to patients. Recent advances in flexible and stretchable electronics could alleviate this issue by exploiting ultrathin form factor to promote intimate, conformable contact of devices to the skin of the submental area (*20*, *21*). However, substantial advances are required for translation of this technology into practice, where factors such as continuous remote data transmission, signal accuracy and reliability, mechanical durability for multiple uses (cost-effectiveness) on a daily or weekly basis, ease of use, and the ability to accommodate patients of any age are all essential.

This circumstance is consistent with the findings of a recent preliminary needs assessment study (table S1), where we interviewed 30 individuals (20 clinicians and 10 patients). Both clinician and patient groups identified poor treatment compliance/adherence as the number one barrier to the rehabilitation of dysphagia. Critically, noncompliance was primarily attributed to high expense, difficult-to-use or limited availability of devices, and inability to access treatment. When asked what components would be most important for an optimal device designed to address these challenges, all clinicians/therapists reported the need for signal accuracy as a critical factor, and all participants (including patients) reported ease of use as a high priority. Therefore, the need to develop and validate easy-to-use, cost-effective, and accurate monitoring systems for the treatment of dysphagia is high.

To address this need, we have developed a mechanically compliant skin sensor patch that is capable of noninvasively interfacing with the submental area in a manner that can be attached and detached multiple times without generating skin irritation and can remotely provide high-fidelity recording of both surface electromyography (sEMG) signals (i.e., muscular activity from submental muscles) and mechanical strain waveforms (i.e., laryngeal/thyroid notch movement) during swallowing.

[1]Weldon School of Biomedical Engineering, Purdue University, West Lafayette, IN 47907, USA. [2]Department of Speech, Language, and Hearing Sciences, Purdue University, West Lafayette, IN 47907, USA. [3]School of Mechanical Engineering, Purdue University, West Lafayette, IN 47907, USA. [4]School of Electrical and Computer Engineering, Purdue University, West Lafayette, IN 47907, USA. [5]Department of Electronics and Communication Engineering, Tezpur University, Assam 784028, India.
*These authors contributed equally to this work.
†Corresponding author. Email: malandraki@purdue.edu (G.M.); lee2270@purdue.edu (C.H.L.)

A precisely designed packaging scheme of the sensor patch, combined with a configuration of open honeycomb networks, provides both elasticity and durability required for multiple usability as a major cost-saving factor. Experimental, computational, and theoretical studies reveal the underlying physical attributes of these design features. Pilot tests on human subjects, including a patient with Parkinson's disease and dysphagia, provide comparable results with those collected using standard clinical sensor systems.

RESULTS

Compliant skin sensor patch system with remote monitoring controls

Figure 1A shows a schematic illustration (left) and a photograph (right) of the system. Here, the sensor patch is mounted to the submental area so that the embedded sEMG electrodes remain in contact with the skin aligned parallel to underlying muscular fibers. The measurement of submental sEMG signals occurs by exploiting double-differential recording using two pairs of recording electrodes (Fig. 1B) with relatively small diameter (5 mm) and interelectrode distance (12 mm) to reduce detection volume and consequently minimize the effect of cross-talk (*22*). In addition, the sensor patch incorporates a strain gauge (Fig. 1C) to provide piezoresistive responses against relative laryngeal movement during swallowing. The sensor patch is connected to a custom-built, portable unit (56 mm × 37 mm × 20 mm, ~55 g) clipped on the wearer's clothing via a flexible anisotropic conductive film wire, allowing for remote data transmission and powering. Figure 1D shows the unpackaged integrated circuit chip of this portable unit that consists of a Bluetooth module (38 mm × 17 mm × 4 mm; HC-06, Guangzhou HC Information Technologies Co. Ltd., China) for remote data

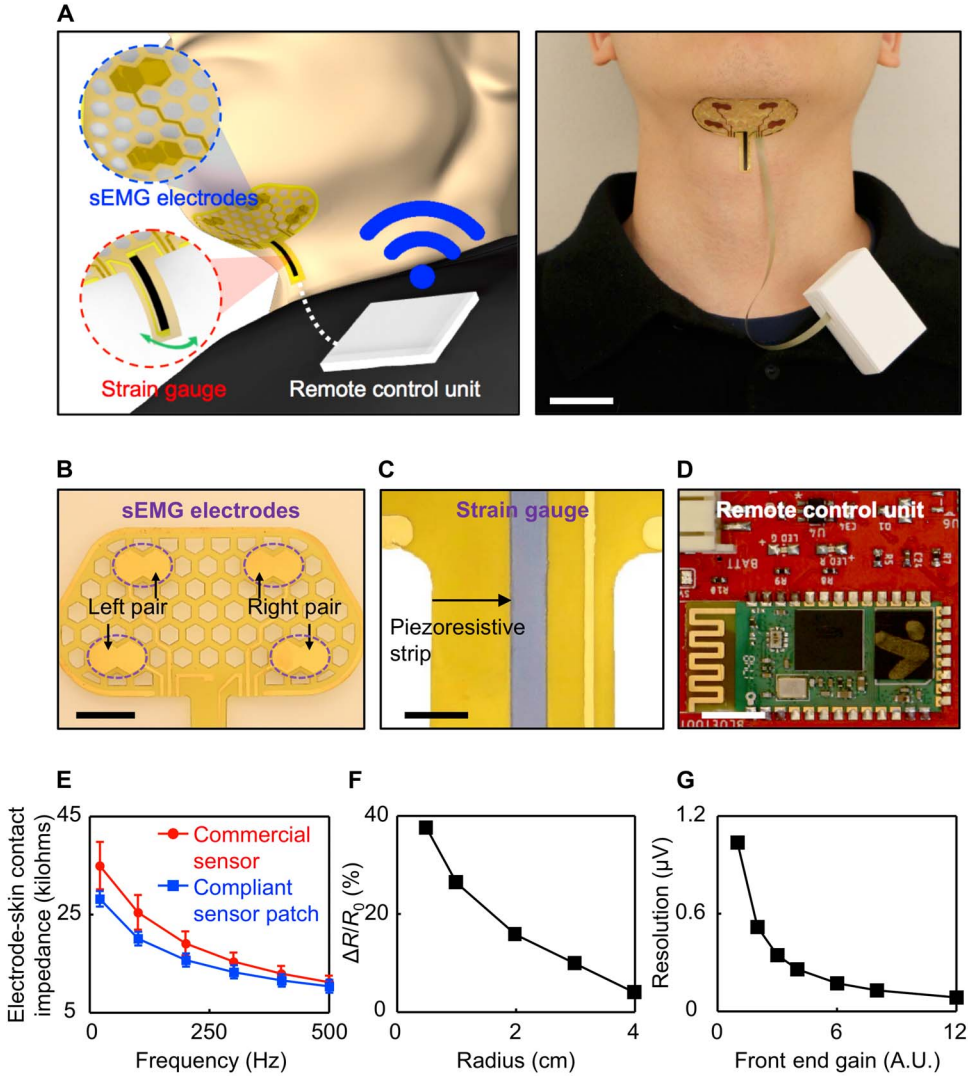

Fig. 1. Basic layouts and configurations of the sensor patch system. (**A**) Schematic illustration (left) and photo (right) of the sensor patch connected with a portable unit clipped on the wearer's clothing for remote data transmission and powering. Scale bar, 2.5 cm. (**B**) Enlarged photo of the sEMG recording electrodes. Scale bar, 1 cm. (**C**) Enlarged photo of the piezoeresistive strip in the strain gauge. Scale bar, 3 mm. (**D**) Photo of the unpackaged integrated circuit chip of the portable unit. Scale bar, 5 mm. (**E**) Measured electrode-skin contact impedances of the compliant recording electrodes (blue plot) by comparison with commercial recording electrodes (red plot). (**F**) Basic characterization of the strain gauge at various bending radii. (**G**) Basic characterization of the remote data transmission unit resolution at various gain settings. A.U., arbitrary units. Photo credit: Min Ku Kim, Purdue University, West Lafayette.

transmission, a four-channel 24-bit analog-to-digital converter (12 mm × 12 mm × 1 mm; ADS1294, Texas Instruments, USA), a rechargeable battery (50 mm × 34 mm × 6 mm, 1000 mAh; PRT-13813, SparkFun Electronics, USA) for on-board power supply, and a three-dimensional (3D)–printed plastic case made of acrylonitrile butadiene styrene for housing.

Comprehensive characterizations for the key components of this sensor patch system indicate the following: (i) the sensor patch provides slightly lower electrode-skin contact impedances than those of commercial recording electrodes (40 mm × 34 mm × 3 mm, Ag/AgCl electrode; Red Dot, 3M), mainly due to the soft, conformal contact along the curvature of the submental area (Fig. 1E); (ii) the strain gauge responds to bending radii of 0.5 to 4 cm (Fig. 1F), and thus remains sensitive to laryngeal/thyroid notch movement during swallowing; (iii) the portable unit allows remote data acquisition across multiple channels at programmable resolution (up to 24 bits) and sampling rate (up to 32 ksps) where the front-end circuit gain is controllable to vary the resolution of the input signal (Fig. 1G).

The fabrication of the sensor patch begins with a thin (13 μm), flexible sheet of polyimide (PI) coated with a Cu film (9 μm) on both sides by geometrically patterning into a configuration of open honeycomb networks with a laser system (PLS6MW, Universal Laser Systems). A subsequent photolithographic patterning, followed by wet etching with a Cu etchant (CE-100, Transene), defines the recording electrodes and interconnectors for two pairs of sEMG channels and a strain gauge on each side of the PI sheet. A piezoresistive strip (Velostat, 3M) is then printed with a conductive adhesive epoxy (#8331, MG Chemicals) to serve as the strain sensing element. The next step involves encapsulating the entire structure with soft elastomers in a core/shell layout that includes (i) an ultralow-modulus elastomer core [Silbione HC2 2022, Bluestar Chemical, ~10-μm thick, Young's modulus (E) = ~5 kPa] to provide physical isolation from the surroundings and (ii) a thin enclosure shell composed of a different elastomer with a modified formulation (Ecoflex, Smooth-On, ~5 μm thick, E = 60 kPa) to provide a mechanically robust, tough interface for handling and lamination. Here, the overall quality of the core/shell layout is determined by controlling the thickness, mechanical modulus, and surface textures of each elastomer layer (*23*). The surface of the recording electrodes remains exposed after the encapsulation where a thin Au film (~500 nm) is electroplated to promote the biocompatibility (*24*). Details of the fabrication process appear in Materials and Methods. These characteristics of the soft core/shell layout allow the sensor patch to remain gently contacted to the submental skin for a range of age groups—between the ages of 26, 35, 45, and 64 years—who have different physical properties of the skin (fig. S1) (*25*, *26*). The contact quality on the submental skin at different age groups—the subject ages of 26 and 79 years—undergoes negligible changes even with head/neck motions and position adjustments of the wearer, and with repetitive placement and removal of the sensor patch, without generating any skin irritation (fig. S2A). The recorded sEMG data during swallowing from these multiple trials (subject age: 26) appear in fig. S2B.

The construction of the sensor patch system occurs by exploiting cost-effective, affordable materials and fabrication methods. Table S2 outlines the estimated costs associated with the constituent electronic components, encapsulation and substrate materials, and processing fees at a laboratory scale, indicating that the total costs for the sensor patch and the portable remote control unit are ~$13.92 and ~$52, respectively. Additional cost savings are expected by reusing the sensor patch multiple times for the same individual through sterilization with 70% ethanol, while the portable remote control unit can be used across multiple patients until the end of its lifetime (years). Here, the sensor patch typically can be reused up to 5 to 10 times without any damage or defect, while the adhesion of the sensor patch to the skin becomes progressively less strong due to dust, sweat, facial hair, or other possible contaminants.

Evaluation of design features in open honeycomb networks

The use of the sensor patch involves its direct attachment onto a curvilinear, dynamic, and anatomically complex body part, i.e., the submental area. For this to be accomplished, the requirements include design features that can provide comfort, resilience, and durability for at least the duration of a swallowing treatment session (typically 45 to 60 min). To realize these physical attributes, the overall structural layout of the sensor patch takes a form of open honeycomb networks (*27*–*30*), providing (i) oxygen permeability through wide-open mesh spaces for skin breathability and comfort, (ii) ability to deform in flexure for intimate contact with the curved surface of the submental area, (iii) density-specific elasticity that can accommodate external loads caused by head/neck movement, and (iv) damage tolerance for which the entire structure can retain its strength and function after minor damages or cuts. Several examples of the sensor patch configured in this way appear in fig. S3, where the characteristic honeycomb lattice length (l) is 2 to 4.5 mm and width (w) is 1 to 6 mm.

Figure 2A presents experimental observation (top) and the corresponding finite element analysis (FEA) results (bottom) obtained with a test bed structure (l = 4.5 mm, w = 1 mm) placed on an artificial skin

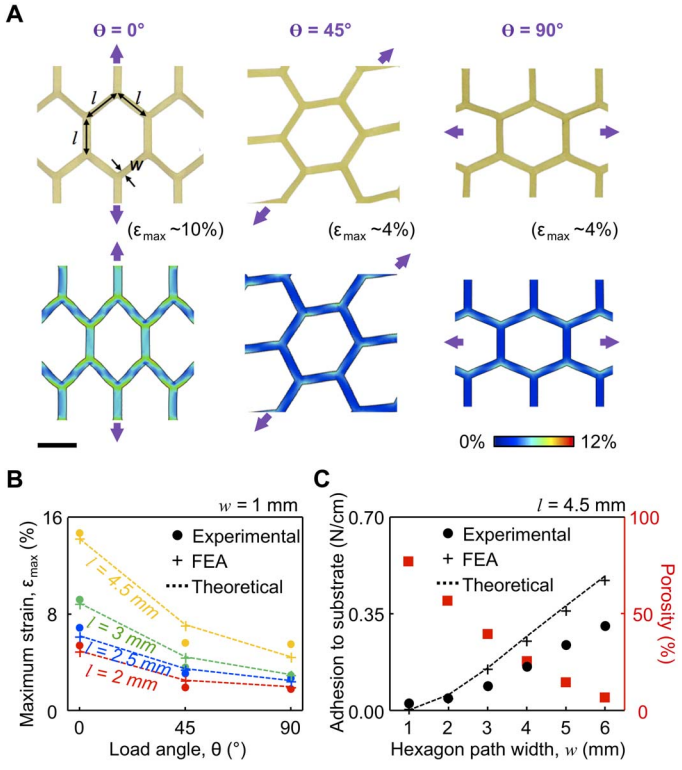

Fig. 2. Key design features of the open honeycomb networks. (**A**) Experimental and computational (FEA) results for a test bed structure under stretching at θ = 0°, 45°, and 90° from the left. Scale bar, 4 mm. (**B**) Experimental, FEA, and theoretical results of the effect of θ on ε_{max} with varied l = 2 to 4.5 mm. (**C**) Experimental, FEA, and theoretical results of the adhesive strength of the test bed structure with varied w = 1 to 6 mm.

substrate (Dragon Skin 30, Smooth-On Inc., 1:1 ratio by weight of parts A and B) under stretching at different loading angles of θ = 0° (left), 45° (middle), and 90° (right) by up to the maximum strain (ε_{max}) of ~10, ~4, and ~4% at the initial delamination of the test bed structure from the substrate. The results consistently confirm that the ε_{max} concentrated at the hexagon edges remains below the limits for plastic deformation of ~16, ~6, and ~8% at θ = 0°, 45°, and 90°, respectively (fig. S4A). Under stretching beyond the ε_{max}, the honeycomb lattices become twisted out of plane to accommodate excessive strains and thereby substantially reduce the contact area (fig. S4B), allowing the wearer to more easily remove the sensor patch from the skin. This feature is especially important for the reusability of the sensor patch because it reduces the risk for skin irritation or damage to the sensor patch. Further enhancement of the stretchability is possible by incorporating state-of-the-art stretchable design layouts, such as filamentary serpentines (*31*), horseshoes (*26*), and self-similar fractals (*32*), into the sensor patch.

Figure 2B presents experimental, computational (FEA), and theoretical results that reveal the effect of θ on ε_{max} before the first crack. At θ = 0°, the ε_{max} remains roughly a factor of two times larger than others at θ = 45° and 90°, yielding consistent results with different values of l = 2 to 4.5 mm. For this reason, the honeycomb lattices are designed to be aligned along the vertical chin surface (θ = 0°) to efficiently accommodate head/neck movement that typically occurs in a vertical rather than horizontal direction during the use and removal of the sensor patch. Comprehensive computational (FEA) results that reveal the underlying mechanics of the honeycomb lattices under these conditions are summarized in fig. S5. Notably, these characteristics are maintained even after several cuts (up to four cuts) of the honeycomb lattices, wherein the electrical conductance is retained through the remaining conduction paths, even under 100 cycles of stretching at the maximum strain of ~16% (fig. S6, A and B).

Intimate physical contact of the sensor patch to the submental skin is particularly important to provide a consistent electrode-skin interface and thereby ensure the attenuated noise from motion artifact (*22*). The adhesive strength of the sensor patch is controlled by modulating the value of w (in turn, porosity), as it changes the effective surface contact area per given unit. Figure 2C provides experimental, computational (FEA), and theoretical results for the adhesive strength of a test bed structure (5.5 cm × 3.3 cm) as a function of w with fixed l = 4.5 mm and θ = 0°, obtained with a mechanical T-peeling tester (resolution, ±5 mN; Mark-10, Copiague, NY) that produces vertical peeling forces at constant rate of 4 mm/min. The increase in w results in monotonous enhancement of the adhesion strength, but at the same time yields reduced total area of open mesh spaces and thereby diminished skin breathability. Representative results of the computational and theoretical analysis for critical stresses (i.e., adhesion strength) at the interface between the skin and the sensor patch with l = 4.5 mm and w = 1 to 6 mm appear in fig. S5B. The results indicate that the sensor patch adheres to the skin wherein the adhesion strength increases as the w increases until the asymptotic limit of approximately 0.27 N/cm for the bulk structure (without the honeycomb networks). These findings provide guidelines for a tailored design of the open honeycomb networks, so that specific requirements and needs (e.g., skin breathability, deformability, and adhesive strength to the skin) for individual patients are met.

Simultaneous remote monitoring of submental muscle activity and laryngeal movement

Simultaneous remote collection of both submental sEMG signals and strain waveforms (representing laryngeal movement) during swallowing and swallowing maneuvers is important in enabling accurate monitoring of swallowing events during the rehabilitation of dysphagia (*33*, *34*). To demonstrate this, we first completed a pilot experiment on a healthy young subject (23-year-old female). Specifically, we attached the sensor patch on the submental skin (after cleaning the surface with a rubbing alcohol wipe and applying a conducting gel to increase electrode-to-skin adherence) and ensured that the recording electrodes were aligned with the submental muscle fibers. The sEMG signals were then collected from the left and right submental muscles during swallows of 5 ml of Varibar thin liquid barium (catalog no. 105, E-Z-EM Canada Inc.) at the sampling rate of 1 kHz with 24-bit resolution and a reference (ground) electrode placed on the mastoid process (behind the ear). The remotely collected sEMG data were comparable to that obtained using a commercial (control) wireless unit (BioRadio, GLNeuroTech Inc.), providing the correlation of >0.95 at the sampling rate of >1 ksps (Nyquist rate) and the analog-to-digital resolution of 12 bit (fig. S6, C and D). Postprocessing of the data was conducted to condition the sEMG signals with a finite impulse response bandpass Butterworth filter at the bandwidth of 20 to 500 Hz. The laryngeal movement during each swallow was simultaneously captured at the superior thyroid notch level (laryngeal prominence) where the strain gauge is located. The information associated with the laryngeal movement allowed us to identify the initiation, relative duration, and completion of a swallow event, which is useful in helping us differentiate the sEMG signals of interest from cross-talk sources originating from surrounding muscles.

Figure 3A (blue) presents the simultaneously recorded submental sEMG signals (top plots) and strain waveforms (bottom plot) during

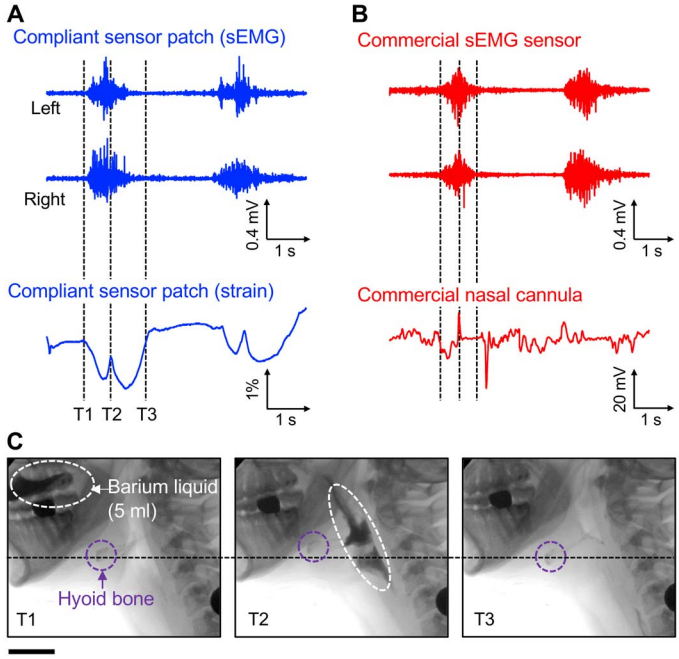

Fig. 3. Pilot study on a healthy young subject (23-year-old female). (**A**) Simultaneously recorded submental sEMG (top two plots) and strain waveforms (bottom plot) during swallows of 5 ml of barium liquid using the compliant sensor patch. (**B**) Simultaneously recorded submental sEMG (top two plots) and strain waveforms (bottom plot) during swallows of 5 ml of barium liquid using conventional commercial recording electrodes and a commercial nasal cannula, respectively. (**C**) A series of screen-captured images from the simultaneous VFSS recording at T1 (left), T2 (middle), and T3 (right). Scale bar, 5.5 cm.

two swallows, recorded remotely via Bluetooth, with comparisons against the control measurements (red). These graphs indicate the amplitude (force generation), duration, and relative onset and offset times of submental muscle activity. The sEMG signals collected via the sensor patch are comparable to those obtained with commercial sEMG recording patches (Red Dot, 3M). The results also show that the "W"-shaped strain waveforms consistently appear during the swallows and represent a rapid upward shift of the thyroid notch and the hyoid bone at the onset of swallowing (T1), followed by an anterior and superior movement to reach the most superior-anterior position (T2), and lastly, return to the original position upon completion of a swallow (T3). Notably, these strain waveforms are effectively distinguishable at lower noise levels than those obtained using a standard nasal airflow cannula to detect swallow apnea (i.e., nasal airflow cessation during swallowing) as a control measurement. Figure 3B presents a series of screen-captured images from a simultaneous videofluoroscopic swallowing study (VFSS) recording at the characteristic time point of T1, T2, and T3, confirming the sequential correlations between the obtained strain waveforms and the thyroid notch and hyoid bone movement. The corresponding VFSS recording appears in movie S1.

Pilot application of the sensor patch system on a patient with dysphagia

To demonstrate feasibility and preliminary clinical validation, a pilot evaluation of the sensor patch system was conducted on a patient with dysphagia. The participant (70-year-old female) was diagnosed with Parkinson's disease (in 2017) and oropharyngeal dysphagia (in 2018). Her dysphagia was primarily characterized by inadequate pharyngeal constriction and reduced lingual strength, resulting in moderate amounts of pharyngeal residue with most consistencies and severe globus sensation (i.e., feeling of food getting stuck in the throat). At the time of her participation in this study, the patient had received 8 weeks of intensive treatment for her swallowing difficulties (*13*). The participant presented with normal cognition. The study took place in a university dysphagia clinic equipped with a videofluoroscopy C-arm system (OEC 9800 Plus Digital Mobile 12″ GE). A certified speech-language pathologist conducted the examination in the presence of a radiation technologist. The participant was seated in an upright position and in view of a laptop that was connected to a BioAmp system (GLNeuroTech Inc.). The researchers attached the sensor patch on the submental skin of the participant, and then the participant was asked to perform two swallows of each of a 5-ml Varibar thin liquid barium (catalog no. 105, E-Z-EM Canada Inc.), 10-ml Varibar thin liquid, and 5 cc Varibar barium pudding (catalog no. 125, E-Z-EM Canada Inc.). The participant was asked to perform additional swallows of 5 ml of Varibar thin liquid barium or 5 cc of Varibar barium pudding during the performance of two well-known swallowing maneuvers. These were the effortful swallows (used to improve pharyngeal constriction and bolus clearance) and the Mendelsohn maneuver (used to improve anterior and superior hyolaryngeal complex movement and upper esophageal sphincter opening) (*35*, *36*). In general, rehabilitation protocols for dysphagia involve performing swallowing exercises to either strengthen the lingual, pharyngeal, and supralaryngeal muscles (*13*), or improve the planning, coordination, and timing of motor aspects of the swallow (i.e., skill-based training approaches) (*37*). During these swallows and swallow maneuvers, submental sEMG signals were captured at the sampling rate of 1 kHz per channel, while the corresponding strain waveforms were simultaneously monitored to identify the relative timing of each swallow event. The swallowing process was further confirmed through simultaneous VFSS recording at full resolution (30 pulses/s) and speed (30 frames/s), along with the use of both a nasal airflow cannula and an observer's button pressing to further confirm the onset of the swallow events.

Figure 4 presents graphical displays of the measured data (black) obtained from the following swallows: 5 ml of liquid using an effortful swallow (Fig. 4A), 5 cc of pudding using an effortful swallow (Fig. 4B), 10 ml of liquid (regular swallow) (Fig. 4C), and 5 ml of liquid using the Mendelsohn maneuver (Fig. 4D), in comparisons with regular (control) swallows of 5 ml of liquid (blue) or 5 cc of pudding (red). The upper and lower hemispheres of each circular graph indicate values of mean normalized amplitude and burst duration of the sEMG signals, respectively. Compared with the corresponding raw data set (fig. S7), this graphical display provides a user-friendly visualization of the amplitude and duration of submental muscle activity, making it easier for patients and clinicians to interpret and visualize the data and obtain biofeedback. These results confirm that the effortful swallows elicited higher submental muscle activity bilaterally (>20% of the patient's maximum) than the regular swallows (<20% of the patient's maximum) for both bolus types, although the effortful liquid swallows required higher amplitude than the pudding trials. The Mendelsohn maneuver elicited both increased amplitude and burst duration of activity compared with the activity elicited by the regular swallows. Amplitude was increased by up to >200% and duration by >270%. Movies S2 to S7 provide the time-synchronized data of the submental sEMG signals and the VFSS recording from these trials. The summary of quantitative analysis of these results appears in fig. S8. The data obtained from these

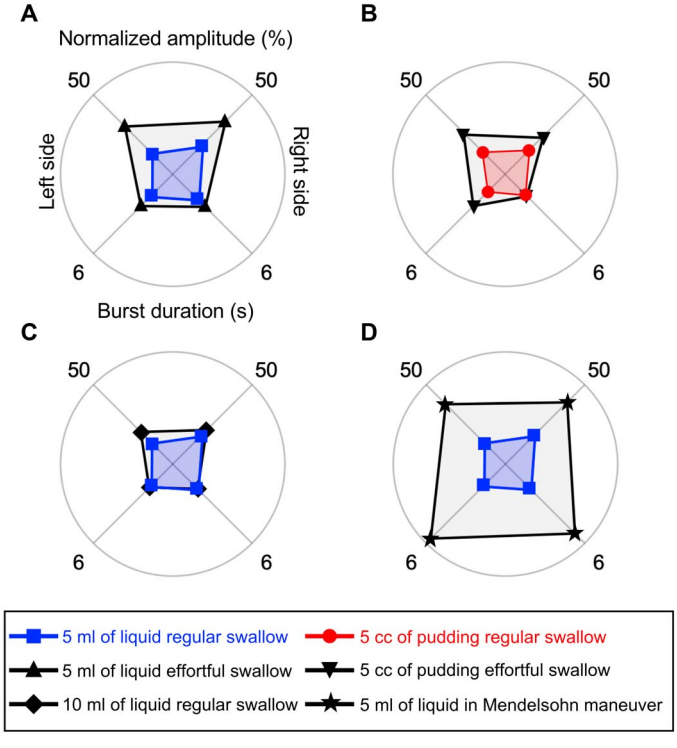

Fig. 4. Pilot study on a patient diagnosed with Parkinson's disease and dysphagia (70-year-old female). Graphical displays (black color) of the measured data obtained from the following swallows: (**A**) 5 ml of liquid using an effortful swallow, (**B**) 5 cc of pudding using an effortful swallow, (**C**) 10 ml of liquid (regular swallow), and (**D**) 5 ml of liquid using the Mendelsohn maneuver, in comparison with regular (control) swallows of 5 ml of liquid (blue color) or 5 cc of pudding (red color).

measurements can provide clinically useful information in terms of identifying neuromuscular impairments (*38*), abnormalities in swallowing muscle activity and duration (*39*), and, more importantly, in providing feedback during swallowing rehabilitation regimens.

DISCUSSION

The results reported here represent preliminary testing and validation of a user-friendly "bandage-like" skin sensor patch platform that is specifically designed for the submental area, and assess both muscle activity and laryngeal/thyroid notch movement during swallowing and swallowing maneuvers. Upon further validation and testing, the flexibly adherent profile and remote monitoring control feature of this platform will allow patients with dysphagia to easily practice their swallowing rehabilitative exercises at home while the data are remotely viewed and assessed in real time by a clinician in the clinic (*40*, *41*). This can potentially minimize the need for repeat clinical visits and allow for optimal telerehabilitation protocols for dysphagia to be developed. The established materials, structures, and configurations of the sensor patch system provide a foundation that can be adjusted and upscaled for extended applications such as the treatment of voice, speech, and other orofacial disorders (*42*), suggesting directions for future research. Extensive clinical evaluations on a large number of patients with dysphagia, which are ongoing, are needed to confirm the use of the sensor patch system across a wide range of age groups and patient diagnoses.

MATERIALS AND METHODS

Fabrication of compliant sensor patch

The entire fabrication process relied on the use of cost-effective rapid-prototyping methods, including photolithographic patterning and laser cutting. The fabrication began by mounting the base substrate of a commercial double-sided Cu clad (Pyralux AP7413R, DuPont USA) composed of a 13-μm-thick PI on a glass slide. The overall outline of the device configurations was patterned using a laser cutter (PLS6MW, Universal Laser Systems), followed by laminating a dry film photoresist (negative type, Riston MM540, DuPont) with a hot roller laminator (AL13P, Apache). The prepared Cu film was then processed under a standard photolithographic patterning that involved an ultraviolet (UV) exposure (0.3 mW/cm^2, Model 18, Jelight Company) for 165 s (50 mJ/cm^2 in total) and soaking in a solution of sodium carbonate (Na_2CO_3) for ~2 min. The UV-exposed Cu film was chemically etched in a solution of ferric chloride ($FeCl_3$) to form the two channels of differential sEMG electrodes and the interconnector traces on the surface. The remaining photoresist was removed by soaking the entire structure in a solution of sodium hydroxide (NaOH) for ~2 min. A piezoresistive strip (sheet resistivity: <30 kilohms/cm^2; Velostat, 3M) was bonded at the preset location using a conductive epoxy adhesive (#8331, MG Chemicals), followed by annealing at 70°C for 30 min in a convection oven. The resulting structure was spin casted with bilayers of silicone elastomers, such as Silbione (HC2 2022, Bluestar Chemical) and Ecoflex (Smooth-On), while the surface of the sEMG recording electrodes was temporarily masked. Curing the elastomers at room temperature overnight, followed by removal of the masking films completed the entire process.

Fabrication of the remote control unit

The portable unit for remote data transmission and powering consisted of two-layer-stacked printed circuit boards (PCBs) with commercially available circuit components. The first layer contained the analog front end on one side and the microcontroller for digital acquisition on the other side. The second layer contained the Bluetooth module and the antenna. The usability (size and battery life) along with the quality of the acquired sEMG signals were the primary constraints taken into account while designing the PCB. The battery life of the device was ~16 hours while transmitting data over the Bluetooth link, which was approximately twice longer than that when using a commercial wireless unit (BioRadio). The size of the portable unit was 5.6 cm × 3.8 cm × 1.8 cm, which is almost three times smaller than that of the commercial unit (10 cm × 6 cm × 2 cm). The data acquisition front-end was programmed in terms of sampling rate and resolution to optimize the condition between the acquisition quality and battery life. The assembled unit was packaged in a 3D-printed housing.

Remote data acquisition

The remote data acquisition was performed by exploiting a zero insertion force connector placed on the board. Both the sEMG signals and strain waveforms were captured during swallowing by a differential input 24-bit resolution analog-to-digital converter (ADS1294, Texas Instrument) at the sampling rates of 1 kHz (sEMG channels) and 100 Hz (strain gauge), respectively. The collected data were then remotely transmitted via a Bluetooth module (HC-06, Guangzhou HC Information Technologies) to an external data acquisition system (commercial smart tablets or phones). The data were then digitally processed with a finite impulse response filter with a fourth-order Butterworth bandpass filter with the cutoff frequency of 20 to 500 Hz and 0.1 to 20 Hz for the recordings of sEMG signals and strain waveforms, respectively.

Finite element analysis

The study to understand the underlying mechanics of the honeycomb-featured structure under mechanical deformations was conducted by using the Abaqus/standard package. The deformation of the structure was modeled by linear elastic behavior with the mechanical modulus (E) of 2.5 GPa and Poisson's ratio of 0.34. The PI substrate was modeled by four-node shell elements (S4R). The refined meshes were used in the numerical calculation to improve accuracy. Displacement boundary conditions were applied to both edges of the structure to produce uniaxial tension for the strains of 4, 8, and 12%. To determine the maximum strain at different angles in Fig. 2B, the empirically obtained data associated with the deformation where the first crack occurs were used.

Theoretical analysis of the stress-strain relationship

Since the stress-strain relationship occurred in the 2D plane until the honeycomb lattices were buckled out of the plane, a MATLAB toolbox (Partial Differential Equation Toolbox, version R2018b) was used to accurately describe the position-resolved anisotropic stress in the system. With the application of a force in various loading directions (Fig. 2A), the stress-strain relation of a material for isotropic and isothermal conditions can be written as

$$\begin{pmatrix} \sigma_x \\ \sigma_y \\ \tau_{xy} \end{pmatrix} = \frac{E}{1-\nu^2} \begin{pmatrix} 1 & \nu & 0 \\ \nu & 1 & 0 \\ 0 & 0 & \frac{1-\nu}{2} \end{pmatrix} \begin{pmatrix} \varepsilon_x \\ \varepsilon_y \\ \gamma_{xy} \end{pmatrix} \quad (1)$$

where σ_x and σ_y are the normal stresses in the x and y are the directions, τ_{xy} is the shear stress, E is the Young's modulus, and ν is

the Poisson's ratio. The deformations along the x and y directions are defined as u and v, respectively. These displacements allowed us to calculate the strain, i.e., $\varepsilon_x = \partial u/\partial x$, $\varepsilon_y = \partial v/\partial y$, $\gamma_{xy} = \partial u/\partial y + \partial u/\partial x$. The force ($k$) in the x and y directions satisfies the equations $-\frac{\partial \sigma_x}{\partial x} - \frac{\partial \tau_{xy}}{\partial y} = k_x$, $-\frac{\partial \tau_{xy}}{\partial x} - \frac{\partial \sigma_y}{\partial y} = k_y$. The displacement equations can be represented in a general form as $-\nabla .\ (c \otimes \nabla u) = k$, where c is a rank 4 tensor, which can be written as four 2 × 2 matrices namely, c_{11}, c_{12}, c_{21}, and c_{22} as

$$c_{11} = \begin{pmatrix} 2G+\mu & 0 \\ 0 & G \end{pmatrix}, c_{12} = \begin{pmatrix} 0 & \mu \\ G & 0 \end{pmatrix}, c_{21} = \begin{pmatrix} 0 & G \\ \mu & 0 \end{pmatrix}, c_{22} = \begin{pmatrix} G & 0 \\ 0 & 2G+\mu \end{pmatrix} \quad (2)$$

where $G = E/2(1 + \nu)$ is the shear modulus and related to μ as $\mu = 2G\nu/(1 - \nu)$. The partial differential equations with the MATLAB toolbox can be solved subject to three types of boundary conditions: (i) Dirichlet—at the edges, the solution u satisfies the equation $hu = r$, which represents a matrix h multiplying the solution vector u, and equaling the vector r. Both h and r can be functions of space (x and y), the solution u, and time. (ii) Neumann boundary conditions—on the edge, the solution u satisfies the equation n. $(c \nabla u) + qu = g$, where n, q, and g (g has the same dimension as k) are the outward unit normal, spring constant, and surface traction respectively. Both q and g can be functions of x, y, the solution u, and, for parabolic and hyperbolic equations, time. Last, (iii) mixed boundary condition involves a combination of Dirichlet and Neumann boundary conditions. In the FEA simulation, the boundary conditions $h_{11} = 1$, $h_{12} = 0$, and $r = 0$ were used as the Dirichlet boundary conditions to fix a hexagon wall in the x direction, and the $q_{11} = 0$ and $q_{12} = 0$ conditions were used as the Neumann boundary conditions (which allows the hexagonal wall to have displacement locally/globally or both). Appropriate force per unit length to have maximum strain was applied to a hexagonal cell wall in a particular load direction through g as Neumann boundary condition.

Theoretical analysis of the maximum strain

The remarkable parametric sensitivity observed in Fig. 2B and predicted by the FEA simulation can be explained by a simple analytical theory as well. Considering that the maximum mechanical strain (ε_{max}) is given by

$$\varepsilon_{max} = \frac{\sigma_{max}}{E} \quad (3)$$

where σ_{max} is the maximum stress that can be sustained by the honeycomb lattice before it breaks, and E is the effective Young's modulus. To recalculate σ_{max}, we note that the honeycomb structure collapses plastically when the bending moment in a unit hexagonal cell wall reached its plastic moment (characterized by a plateau of the stress-strain curve). Therefore, σ_{max} was calculated by (*43*)

$$\sigma_{plastic} = \sigma_{ys} \left(\frac{w}{l}\right)^2 \frac{1}{2(h/l + \sin\theta)\ \sin\ \theta} \quad (4)$$

where σ_{ys} is the yield strength of the PI material. Similarly, the anisotropic Young's modulus of the hexagonal PI (E) was calculated as

$$E = E_{poly} \left(\frac{w}{l}\right)^3 \frac{\cos\theta}{(h/l + \sin\theta)\sin^2\theta} \quad (5)$$

where E_{poly} is the Young's modulus of the PI, and h, l, and w are the height, length, and width of the hexagon wall. To interpret the experimental results, we considered four regular honeycomb lattices (w = 1 mm, $h = l$ = 2, 2.5, 3, and 4.5 mm as in fig. S3) loaded in three different directions (θ = 0°, 45°, and 90°). The largest section of the honeycomb lattice having the l of 70 mm and the w of 20 mm was simulated to eliminate any edge effect. The force with which a hexagonal wall is pulled normally in the outward direction is F_n. Therefore, when the lattice is pulled in the positive x direction (θ = 90°), each right vertical wall of the honeycomb is pulled by a force F_n, and each outside sidewall contributes a force of $F_n \cos(60°)$ (=0.5 F_n), and the total force acting on the honeycomb walls of the lattice (F_x) is the sum of the individual forces on the nonoverlapping hexagon walls residing in the extreme right side of the x direction in a width of 20 mm of the lattice. However, when a force is applied in the vertical direction (θ = 0°), each hexagon cell has two side walls in the force direction each contributing a force of $F_n \cos(30°)$ in the θ = 0° loading direction. Therefore, each hexagon contributes a force of $2F_n \cos(30°)$ (=1.73 F_n) along the θ = 0° loading direction. As the length of the lattice is 70 mm, the number of hexagon walls contributing to total force in the θ = 0° direction (F_y) is more than θ = 90° loading direction (> or ~2 times depending on the hexagon wall length and width dimension). As the total area and the Young's modulus (E, for a fixed value of l) of the PI substrate remain same, with an increased value of applied force, the strain is more for the θ = 0° load direction compared with the strain in the θ = 90° load direction. As the maximum strain is directly proportional to the maximum force applied to the lattice (Eq. 3), loading the lattice in the θ = 0° axis has the maximum strain than loading along any other direction. Similarly, we calculated the force components along the θ = 45° load direction and the corresponding maximum strain as well. Equations 3 and 4 accurately predicted the FEA simulation.

Theoretical analysis of adhesion force

Since the FEA results were captured by the analytical theory, we also calculated the adhesion using the analytical theory. Considering the adhesion properties of a honeycomb lattice affixed onto a substrate, the adhesion force between a 10-μm-thick layer of Silbione (HC2 2022) and a 13-μm-thick PI was calculated by placing the Silbione layer on a 500-μm-thick Si wafer and then slowly pulling the PI film in the outward direction. The length and width of PI substrate are 65 and 38 mm, respectively. The effective Young's modulus (E_{eff}) of the Si wafer and the Silbione was calculated as (*44*)

$$E_{eff} = V_1E_1 + V_2E_2 + \frac{V_1V_2E_1E_2(\nu_1 - \nu_2)^2}{V_1E_1(1 - \nu_2^2) + V_2E_2(1 - \nu_1^2)} \quad (6)$$

where V_1 and V_2 are the volume fractions, E_1 and E_2 are the Young's moduli, and ν_1 and ν_2 are the Poisson's ratios of the Si wafer and the Silbione, respectively. The adhesion force per width between the Silbione and the PI was computed using the Timoshenko model as (*45*)

$$F_{adhesion} = \frac{-\varepsilon_m}{1/E_{eff}t_1 + 1/E_{poly}t_2 + 3(t_1 + t_2)^2/(E_{eff}t_1^3 + E_{poly}t_2^3)} \quad (7)$$

where t_1 and t_2 are thicknesses of the Silbione and PI, respectively. $\varepsilon_m = \varepsilon_f - \varepsilon_S$, ε_f and ε_S are the strains induced by lattice mismatch in the Silbione and PI, respectively. ε_m is the mismatch strain defined as

$\varepsilon_m = (a_s - a_f)/a_f$, where a_f and a_s are the lattice parameters of the Silbione and PI, respectively. The following material constants were used in the computation: E_{Si} = 179 GPa (Si <100>, single crystal, undoped), $E_{Silbione}$ = 5 kPa (HC2 2022, Bluestar Chemical), E_{PI} = 4.826 GPa (Pyralux AP7413R, DuPont USA), ν_{Si} = 0.265, and $\nu_{Silbione}$ = 0.48. The adhesion force was calculated for PI having a hexagon cell wall length (l) of 4.5 mm and a width (w) of 1 to 6 mm. The theoretical predictions provided a good agreement with the experimental results in Fig. 2C.

Computational analysis of adhesion force

For the computational modeling in fig. S5, the sensor patch was contacted to the skin with a clinically accepted adhesive material (~10 μm thick, E = ~5 kPa; Silbione HC2 2022, Bluestar Chemical). The parameters for the thickness, E, and Poisson ratio of the skin are 0.2 mm, 10 MPa, and 0.49, respectively. The effective E of the sensor patch was determined using Eq. 6. The lattice mismatch constant (ε_m) at the interface was obtained from a previous experimental study for adhesion force between the skin and Silbione (*46*). For the 3D FEM analysis (using the commercial software COMSOL), a series of open honeycomb lattices with l = 4.5 mm and w = 1 to 6 mm were considered. For each unit cell, a peeling force was applied at the edge of the honeycomb lattice while the maximum strain developed at the interface was recorded. The corresponding stress-strain curve was obtained to determine the stress at which the maximum strain reached a critical value. The results showed that the sensor patch adhered well to the skin in which the adhesion strength increases with w. The asymptotic limit of the adhesion force ($F_{adhesion}$) between the sensor patch and the skin for the bulk structure (without the honeycomb networks) was obtained when the honeycomb meshes were closed at $w \to \sqrt{3} \cdot l$, and its value is approximately 0.27 N/cm. These results were comparable to those obtained on the basis of the recent analytical expression for the E of honeycomb networks (*47*)

$$E = E_{poly}\left(\frac{w}{l}\right)^3 \frac{\sin\theta}{\frac{h}{l}(1+\cos\theta)\left(\sin^2\theta\left(\frac{w}{l}\right)^2 + \cos^2\theta\right)} \quad (8)$$

VFSS recording

The VFSS images were acquired using a videofluoroscopic C-arm system (OEC 9800 Plus Digital Mobile 12" GE) at the full resolution (30 pulses/s) and recorded at 30 frames/s on an MDR digital video recorder (PACSgear). The patient was seated in an upright position in lateral view to allow visualization of the lips, oral and nasal cavities, cervical vertebrae, and the upper esophagus. The following swallowing trials were performed (two times each): 5 ml of Varibar thin liquid barium (catalog no. 105, E-ZEM Canada Inc.), 10 ml of Varibar thin liquid, and 5 cc of Varibar barium pudding (catalog no.125, E-Z-EM Canada Inc.). In addition, the patient was asked to perform additional swallows of 5 ml of Varibar thin liquid barium or 5 cc of Varibar barium pudding using the following commonly prescribed swallowing maneuvers/exercises that are often trained with the use of sEMG: effortful swallow (or "swallow hard") and Mendelsohn maneuver (or "swallow longer"). Barium was used as the contrast because it is visible in videofluoroscopy.

Analysis of sEMG signals and strain waveforms

The sEMG recordings were analyzed using a custom-built MATLAB code (MATLAB Inc., Natick, MA). The sEMG signals were calibrated, and the raw signals were demeaned, rectified, and smoothed. The measurements obtained from each trial were (i) amplitude (area under the curve) and (ii) burst duration of the smoothed sEMG signals for the left and right channels. After preprocessing, the onsets and offsets of each trial were selected to calculate the sEMG amplitude and burst duration. Identification of swallow events was semiautomatic. The analyzer identified the trial of interest and the relative onset and offset of the swallow. Within the user-selected window, an algorithm was applied to determine the onset and offset of EMG activity (defined as a change in sEMG amplitude that was >2 SDs of the pretrial sEMG baseline activity) and within 0.5 s of the user-defined window. In addition, because sEMG amplitudes vary between tasks and subjects (e.g., as a function of electrode impedance), sEMG amplitude in microvolts was normalized relative to the amplitude recorded during the maximal voluntary contraction. Specifically, the patient who participated in this pilot study produced three trials of maximum lingual press using the Iowa Oral Performance Instrument, and we expressed the task-related sEMG amplitudes as percentages of the mean amplitude of this criterion gesture.

SUPPLEMENTARY MATERIALS

Supplementary material for this article is available at http://advances.sciencemag.org/cgi/content/full/5/12/eaay3210/DC1

Fig. S1. Sensor patch adhered to the human submental skin of different ages.
Fig. S2. Repeated use of the submental sensor patch.
Fig. S3. Hexagonal test bed geometrical variation.
Fig. S4. Hexagonal test bed under mechanical loads.
Fig. S5. Mechanical simulation of test bed structures under mechanical loads.
Fig. S6. Electrical reliability and performance comparison.
Fig. S7. Swallowing treatment session results.
Fig. S8. Swallowing treatment session data analysis.
Table S1. Initial needs assessment survey.
Table S2. Cost estimation of the submental sensor patch system.
Movie S1. Pilot VFSS recording of a swallow.
Movie S2. sEMG, strain, and VFSS recordings of a swallowing treatment session.
Movie S3. sEMG, strain, and VFSS recordings of a swallowing treatment session.
Movie S4. sEMG, strain, and VFSS recordings of a swallowing treatment session.
Movie S5. sEMG, strain, and VFSS recordings of a swallowing treatment session.
Movie S6. sEMG, strain, and VFSS recordings of a swallowing treatment session.
Movie S7. sEMG, strain, and VFSS recordings of a swallowing treatment session.

View/request a protocol for this paper from *Bio-protocol*.

REFERENCES AND NOTES

1. A. L. Perlman, P. M. Palmer, T. M. McCulloch, D. J. Vandaele, Electromyographic activity from human laryngeal, pharyngeal, and submental muscles during swallowing. *J. Appl. Physiol.* **86**, 1663–1669 (1999).
2. P. Sörös, Y. Inamoto, R. E. Martin, Functional brain imaging of swallowing: An activation likelihood estimation meta-analysis. *Hum. Brain Mapp.* **30**, 2426–2439 (2009).
3. G. A. Malandraki, B. P. Sutton, A. L. Perlman, D. C. Karampinos, C. Conway, Neural activation of swallowing and swallowing-related tasks in healthy young adults: An attempt to separate the components of deglutition. *Hum. Brain Mapp.* **30**, 3209–3226 (2009).
4. N. Bhattacharyya, The prevalence of dysphagia among adults in the United States. *Otolaryngol. Head Neck Surg.* **151**, 765–769 (2014).
5. N. Bhattacharyya, The prevalence of pediatric voice and swallowing problems in the United States. *Laryngoscope* **125**, 746–750 (2015).
6. K. A. Hutcheson, J. S. Lewin, D. A. Barringer, A. Lisec, G. B. Gunn, M. W. S. Moore, F. C. Holsinger, Late dysphagia after radiotherapy-based treatment of head and neck cancer. *Cancer* **118**, 5793–5799 (2012).
7. L. Rofes, N. Vilardell, P. Clavé, Post-stroke dysphagia: Progress at last. *Neurogastroenterol. Motil.* **25**, 278–282 (2013).
8. S. E. Langmore, K. A. Skarupski, P. S. Park, B. E. Fries, Predictors of aspiration pneumonia in nursing home residents. *Dysphagia* **17**, 298–307 (2002).
9. L. W. J. Baijens, P. Clave, P. Cras, O. Ekberg, A. Forster, G. F. Kolb, J. C. Leners, S. Masiero, J. Mateos-Nozal, O. Ortega, D. G. Smithard, R. Speyer, M. Walshe, European Society for

Swallowing Disorders–European Union Geriatric Medicine Society white paper: Oropharyngeal dysphagia as a geriatric syndrome. *Clin. Interv. Aging* **11**, 1403–1428 (2016).
10. M. A. Crary, G. D. Carnaby, L. A. LaGorio, P. J. Carvajal, Functional and physiological outcomes from an exercise-based dysphagia therapy: A pilot investigation of the McNeill Dysphagia Therapy Program. *Arch. Phys. Med. Rehabil.* **93**, 1173–1178 (2012).
11. J. Robbins, S. A. Kays, R. E. Gangnon, J. A. Hind, A. L. Hewitt, L. R. Gentry, A. J. Taylor, The effects of lingual exercise in stroke patients with dysphagia. *Arch. Phys. Med. Rehabil.* **88**, 150–158 (2007).
12. B. Martin-Harris, D. McFarland, E. Hill, C. Strange, K. Focht, Z. Wan, J. Blair, K. McGrattan, Respiratory-swallow training in patients with head and neck cancer. *Arch. Phys. Med. Rehabil.* **96**, 885–893 (2015).
13. G. Malandraki, A. Rajappa, C. Kantarcigil, E. Wagner, C. Ivey, K. Youse, The intensive dysphagia rehabilitation approach applied to patients with neurogenic dysphagia: A case series design study. *Arch. Phys. Med. Rehabil.* **97**, 567–574 (2016).
14. Health Resources & Services Administration, Defining rural population, (2015); http://www.hrsa.gov/ruralhealth/policy/definition_of_rural.html.
15. B. N. Krekeler, C. K. Broadfoot, S. Johnson, N. P. Connor, N. Rogus-Pulia, Correction to: Patient adherence to dysphagia recommendations: A systematic review. *Dysphagia* **33**, 589–591 (2018).
16. W.-Y. Shieh, C.-M. Wang, C.-S. Chang, Development of a portable non-invasive swallowing and respiration assessment device. *Sensors* **15**, 12428–12453 (2015).
17. E. Sazonov, S. Schuckers, P. Lopez-Meyer, O. Makeyev, N. Sazonova, E. L. Melanson, M. Neuman, Non-invasive monitoring of chewing and swallowing for objective quantification of ingestive behavior. *Physiol. Meas.* **29**, 525–541 (2008).
18. T. Ono, K. Hori, Y. Masuda, T. Hayashi, Recent advances in sensing oropharyngeal swallowing function in Japan. *Sensors* **10**, 176–202 (2010).
19. Y. Tajitsu, A. Suehiro, K. Tsunemine, K. Katsuya, Y. Kawaguchi, Y. Kuriwaki, Y. Sugino, H. Nishida, M. Kitamura, K. Omori, Application of piezoelectric braided cord to dysphagia-detecting system. *Jpn. J. Appl. Phys.* **57**, 11UG02 (2018).
20. Y. Lee, B. Nicholls, D. S. Lee, Y. F. Chen, Y. Chun, C. S. Ang, W. H. Yeo, Soft electronics enabled ergonomic human-computer interaction for swallowing training. *Sci. Rep.* **7**, 46697 (2017).
21. G. Constantinescu, J. W. Jeong, X. D. Li, D. K. Scott, K. I. Jang, H. J. Chung, J. A. Rogers, J. Rieger, Epidermal electronics for electromyography: An application to swallowing therapy. *Med. Eng. Phys.* **38**, 807–812 (2016).
22. C. Stepp, Surface electromyography for speech and swallowing systems: Measurement, analysis, and interpretation. *J. Speech Lang. Hear. Res.* **55**, 1232–1246 (2012).
23. C. H. Lee, Y. Ma, K.-I. Jang, A. Banks, T. Pan, X. Feng, J. Kim, D. Kang, M. Raj, B. McGrane, B. Morey, X. Wang, R. Ghaffari, Y. Huang, J. Rogers, Soft core/shell packages for stretchable electronics. *Adv. Funct. Mater.* **25**, 3698–3704 (2015).
24. M. Vafaiee, M. Vossoughi, R. Mohammadpour, P. Sasanpour, Gold-plated electrode with high scratch strength for electrophysiological recordings. *Sci. Rep.* **9**, 2985 (2019).
25. V. Mazzarello, M. Ferrari, P. Ena, Werner syndrome: Quantitative assessment of skin aging. *Clin. Cosmet. Investig. Dermatol.* **11**, 397–402 (2018).
26. K.-I. Jang, H. U. Chung, S. Xu, C. H. Lee, H. Luan, J. Jeong, H. Cheng, G.-T. Kim, S. Y. Han, J. W. Lee, J. Kim, M. Cho, F. Miao, Y. Yang, H. N. Jung, M. Flavin, H. Liu, G. W. Kong, K. Yu, S. I. Rhee, J. Chung, B. Kim, J. Kwak, M. H. Yun, J. Y. Kim, Y. Song, U. Paik, Y. Zhang, Y. Huang, J. A. Rogers, Soft network composite materials with deterministic and bio-inspired designs. *Nat. Commun.* **6**, 6566 (2015).
27. C. M. Taylor, C. W. Smith, W. Miller, K. E. Evans, The effects of hierarchy on the in-plane elastic properties of honeycombs. *Int. J. Solids Struct.* **48**, 1330–1339 (2011).
28. D. Mousanezhad, B. Haghpanah, R. Ghosh, A. M. Hamouda, H. Nayeb-Hashemi, A. Vaziri, Elastic properties of chiral, anti-chiral, and hierarchical honeycombs: A simple energy-based approach. *Theor. App. Mech. Lett.* **6**, 81–96 (2016).
29. Y. P. Liu, H. Hu, A review on auxetic structures and polymeric materials. *Sci. Res. Essays* **5**, 1052–1063 (2010).
30. T. Takahashi, K. Takei, A. Gillies, R. Fearing, A. Javey, Carbon nanotube active-matrix backplanes for conformal electronics and sensors. *Nano Lett.* **11**, 5408–5413 (2011).
31. J. Kim, M. Lee, H. J. Shim, R. Ghaffari, H. R. Cho, D. Son, Y. H. Jung, M. Soh, C. Choi, S. Jung, K. Chu, D. Jeon, S.-T. Lee, J. H. Kim, S. H. Choi, T. Hyeon, D.-H. Kim, Stretchable silicon nanoribbon electronics for skin prosthesis. *Nat. Commun.* **5**, 5747 (2014).
32. J. Fan, W.-H. Yeo, Y. Su, Y. Hattori, W. Lee, S.-Y. Jung, Y. Zhang, Z. Liu, H. Cheng, L. Falgout, M. Bajema, T. Coleman, D. Gregoire, R. Larsen, Y. Huang, J. A. Rogers, Fractal design concepts for stretchable electronics. *Nat. Commun.* **5**, 3266 (2014).
33. K. M. Wheeler-Hegland, J. C. Rosenbek, C. M. Sapienza, Submental sEMG and hyoid movement during mendelsohn maneuver, effortful swallow, and expiratory muscle strength training. *J. Speech Lang. Hear. Res.* **51**, 1072–1087 (2008).
34. Q. Li, K. Hori, Y. Minagi, T. Ono, Y.-j. Chen, J. Kondo, S. Fujiwara, K. Tamine, H. Hayashi, M. Inoue, Y. Maeda, Development of a system to monitor laryngeal movement during swallowing using a bend sensor. *PLOS ONE* **8**, e70850 (2013).
35. S. H. Doeltgen, E. Ong, I. Scholten, C. Cock, T. Omari, Biomechanical quantification of mendelsohn maneuver and effortful swallowing on pharyngoesophageal function. *Otolaryngol. Head Neck Surg.* **157**, 816–823 (2017).
36. G. H. McCullough, E. Kamarunas, G. C. Mann, J. W. Schmidley, J. A. Robbins, M. A. Crary, Effects of Mendelsohn maneuver on measures of swallowing duration post stroke. *Top. Stroke Rehabil.* **19**, 234–243 (2012).
37. R. P. Athukorala, R. D. Jones, O. Sella, M. L. Huckabee, Skill training for swallowing rehabilitation in patients With Parkinson's disease. *Arch. Phys. Med. Rehabil.* **95**, 1374–1382 (2014).
38. H. M. Clark, Neuromuscular treatments for speech and swallowing: A tutorial. *Am. J. Speech Lang. Pathol.* **12**, 400–415 (2003).
39. C.-M. Wang, W.-Y. Shieh, Y.-H. Weng, Y.-R. Wu, Non-invasive assessment determine the swallowing and respiration dysfunction in early Parkinson's disease. *Parkinsonism Relat. Disord.* **42**, 22–27 (2017).
40. C. Kantarcigil, G. A. Malandraki, First step in telehealth assessment: A randomized controlled trial to investigate the effectiveness of an electronic case history form for dysphagia. *Dysphagia* **32**, 548–558 (2017).
41. C. Kantarcigil, J. J. Sheppard, A. M. Gordon, K. M. Friel, G. A. Malandraki, A telehealth approach to conducting clinical swallowing evaluations in children with cerebral palsy. *Res. Dev. Disabil.* **55**, 207–217 (2016).
42. D. S. Chung, C. Wettroth, M. Hallett, C. W. Maurer, Functional speech and voice disorders: Case series and literature review. *Mov. Disord. Clin. Pract.* **5**, 312–316 (2018).
43. L. J. Gibson, M. F. Ashby, *Cellular Solids: Structure and Properties* (Cambridge Univ. Press, ed. 2, 1997).
44. B. Liu, X. Feng, S.-M. Zhang, The effective Young's modulus of composites beyond the Voigt estimation due to the Poisson effect. *Compos. Sci. Technol.* **69**, 2198–2204 (2009).
45. Y. Zhang, Extended Stoney's formula for a film-substrate bilayer with the effect of interfacial slip. *J. Appl. Mech.* **75**, 011008 (2008).
46. L. Liu, K. Kuffel, D. K. Scott, G. Constantinescu, H.-J. Chung, J. Rieger, Silicone-based adhesives for long-term skin application: Cleaning protocols and their effect on peel strength. *Biomed. Phys. Eng. Express* **4**, 015004 (2018).
47. R. Hedayati, M. Sadighi, M. M. Aghdam, A. A. Zadpoor, Mechanical properties of additively manufactured thick honeycombs. *Materials* **9**, E613 (2016).

Acknowledgments: All studies on human subjects were approved through the Purdue Institutional Review Board (protocol nos. 1605017777 and 1807020788) and conducted in compliance with applicable regulations. **Funding:** This work was supported by grants from the NIH National Institute of Biomedical Imaging and Bioengineering (NIBIB: 1R21EB026099-01A1), Showalter Trust Research Award, Purdue Institute for Integrative Neuroscience, the Purdue Research Foundation, and the Purdue Department of Speech, Language, and Hearing Sciences. R.K.B. is funded by the Department of Biotechnology, India, with sanction no. BT/20/NE/2011 (01/08/2017). S.S. is funded by the NSF CRII Award: CNS 1657455. **Author contributions:** C.H.L. and G.M. conceived, designed, and led the experiments. M.K.K., C.K., B.K., Y.P., S.M., K.K., S.L., J.B.M., S.A., S.S., G.M., and C.H.L. performed the experiments and analyzed the data. R.K.B., B.K., and M.A.A. performed the modeling. M.K.K., C.K., R.K.B., B.K., S.M., A.S., S.S., M.A.A., G.M., and C.H.L. wrote the paper. All authors discussed the results and edited the manuscript at all stages. **Competing interests:** C.H.L. and G.M. are inventors on patents related to this work filed by Purdue University Office of Technology Commercialization (no. 62/595,345, filed 6 December 2017; no. 15/876,977, filed 22 January 2018). C.H.L. and G.M. formed a startup company (Curasis LLC). The authors declare that they have no other competing interests. **Data and materials availability:** All data needed to evaluate the conclusions in the paper are present in the paper and/or the Supplementary Materials. Additional data related to this paper may be requested from the authors.

Submitted 8 June 2019
Accepted 10 October 2019
Published 13 December 2019
10.1126/sciadv.aay3210

Citation: M. K. Kim, C. Kantarcigil, B. Kim, R. K. Baruah, S. Maity, Y. Park, K. Kim, S. Lee, J. B. Malandraki, S. Avlani, A. Smith, S. Sen, M. A. Alam, G. Malandraki, C. H. Lee, Flexible submental sensor patch with remote monitoring controls for management of oropharyngeal swallowing disorders. *Sci. Adv.* **5**, eaay3210 (2019).